UC Berkeley
UC Berkeley Previously Published Works

Title

Study of Variation Mechanisms of the Martian Diffuse Aurora Based on Monte Carlo Simulations and MAVEN Observations

Permalink

https://escholarship.org/uc/item/20r907bx

Journal

Journal of Geophysical Research Space Physics, 130(2)

ISSN

2169-9380

Authors

Okiyama, Taishin

Seki, Kanako

Nakamura, Yuki

et al.

Publication Date

2025-02-01

DOI

10.1029/2024ja033420

Peer reviewed

Study of Variation Mechanisms of the Martian Diffuse Aurora Based on Monte Carlo Simulations and MAVEN Observations

Taishin Okiyama[1], **Kanako Seki[1]**, **Yuki Nakamura[1]**, **Robert J. Lillis[2]**, **Ali Rahmati[2]**, **Davin E. Larson[2]**, **Gina A. DiBraccio[3]**, **Nicholas M. Schneider[4]**, **Sonal K. Jain[4]**, **Ryoya Sakata[5]**, and **Shannon Curry[4]**

[1]Department of Earth and Planetary Science, Graduate School of Science, University of Tokyo, Tokyo, Japan, [2]Space Sciences Laboratory, University of California, Berkeley, CA, USA, [3]NASA Goddard Space Flight Center, Greenbelt, MD, USA, [4]Laboratory for Atmospheric and Space Physics, University of Colorado at Boulder, Boulder, CO, USA, [5]Department of Geophysics, Graduate School of Science, Tohoku University, Sendai, Japan

Abstract Martian diffuse auroras are ultraviolet emissions spread across the nightside of Mars caused by solar energetic particles (SEP), both electrons and protons. The nightside structures of induced and crustal magnetic fields are expected to affect the diffuse auroral emission profiles caused by electrons, which is far from understood. Here we estimate magnetic field effects on emission based on a newly developed Monte Carlo model simulating collisions and electron cyclotron motions. Parameter surveys of the magnetic field intensity and dip angle (angle of magnetic field line from horizontal direction) under uniform magnetic field structure show that the effects of magnetic field dip angle on auroral altitude profiles are greater than those of magnetic field intensity. We then applied our model to the September 2017 diffuse aurora event using MAVEN SEP electron flux observations and neutral atmospheric profile from the Mars Climate Database as inputs. Comparison between horizontal and vertical magnetic field dip angle cases indicates that the horizontal dip angle case results in broader limb-integrated auroral altitude profiles than the vertical case and enhances the auroral intensity at high altitudes (>75 km). The magnetic field structure can be one of the important factors in understanding the Martian diffuse auroras.

Plain Language Summary Martian diffuse auroras are ultraviolet emissions spread across the nightside of Mars caused by high-energy electrons and protons from the Sun. The diffuse auroral emissions caused by electrons are expected to vary with nightside magnetic field structures around Mars. However, the effects of the magnetic fields on diffuse auroral emission profiles are far from understood. This study shows an estimation of the magnetic field effects based on a newly developed model and spacecraft observations. The model results under uniform magnetic field assumptions show that the effects of magnetic field directions on auroral altitude profiles are greater than those of magnetic field intensity, and the more horizontal magnetic fields result in broader auroral altitude profiles. The magnetic field structure can be one of the important factors in understanding the Martian diffuse auroras.

1. Introduction

Mars does not have a global intrinsic magnetic field, but locally strong, inhomogeneous crustal remanent magnetic fields rotate with the planet (Acuña et al., 1999; Connerney et al., 2005). The solar wind encounters the conducting obstacle of Mars' dayside ionosphere, causing the interplanetary magnetic field to pileup and drape around Mars in an induced magnetosphere (Halekas et al., 2021). The induced magnetic field structures are variable, especially during extreme solar events such as interplanetary coronal mass ejections (ICME) arrival. During the ICME event in September 2017, the induced magnetic field strength and structures significantly changed (e.g., Harada et al., 2018; Xu et al., 2018). The model studies show complicated and changing induced magnetic field structures during the ICME event (Luhmann et al., 2017; Ma et al., 2018; Xu et al., 2018). However, it is difficult to investigate the global magnetic field structures by observations during ICME events because the statistical average using point measurements of spacecraft observations does not necessarily represent the extreme cases. Despite these difficulties, the induced magnetic field structures during ICME events are important. The magnetic fields in the near-Mars environment determine charged particle motions and can control the atmospheric evolution through atmospheric ion escape (e.g., Jakosky et al., 2015).

Martian diffuse aurora is the global ultraviolet emissions in the nightside upper atmosphere of Mars, which was discovered by the Imaging Ultraviolet Spectrograph (IUVS) onboard the Mars Atmosphere and Volatile EvolutioN (MAVEN) spacecraft (Schneider et al., 2015, 2018). One of the main emission lines is the CO_2^+ ultraviolet doublet (UVD), which peaks at altitudes around 70 km and is possibly excited by high energy electrons around hundreds of keV or protons around a few MeV called as solar energetic particles (SEP) (Gérard et al., 2017; Haider & Masoom, 2019; Nakamura et al., 2022; Schneider et al., 2015). SEPs causing Martian diffuse auroras are produced by solar eruptions and successive acceleration around the interplanetary shocks with ICME (Temmer, 2021). SEPs can precipitate globally into the Martian atmosphere and cause global auroral emissions.

The effects of the magnetic fields on the transport of SEP electrons and protons are different due to the difference in their cyclotron radius. SEP protons with energies around MeV have large cyclotron radius comparable to Mars' radius and are not expected to be affected by the induced magnetic fields around Mars, though shadowing by the planet is important for proton precipitation (Afonin et al., 1989; Kallio et al., 2012; Lillis et al., 2016; Luhmann et al., 2007; McKenna-Lawlor et al., 2012). In contrast, auroral emission altitude profiles produced by the electrons are expected to vary with changes in the magnetic fields because the electrons are magnetized and precipitate into the Martian atmosphere along the magnetic field lines. For example, the gyroradii of 100 keV electron with 40° pitch angle in 10 and 100 nT background magnetic field are 72 and 7.2 km, respectively. Jolitz et al. (2021) showed that the precipitation regions of SEP electrons are affected by the induced magnetic field, but the variations of auroral emission altitude profiles by the induced magnetic fields have not yet been investigated.

There are several model studies about Martian diffuse auroral emissions. Schneider et al. (2015) applied the Atmospheric Ultraviolet Radiance Integrated Code based on the multi-stream method, which was originally developed for modeling the airglow of the Earth (Strickland et al., 1999). Gérard et al. (2017) applied the Monte Carlo electron transport model based on the direct simulation Monte Carlo method (Shematovich et al., 1994, 2008) to reproduce the Martian diffuse auroras. Haider and Masoom (2019) used a hybrid model and a four-dimensional yield spectrum approach based on Monte Carlo simulation, which includes not only energetic electrons but also the solar wind protons and hydrogen in the Martian corona. Nakamura et al. (2022) developed a Monte Carlo model solving the transport of energetic electrons and protons and showed energetic protons above MeV produce a lower auroral emission peak around 50–70 km than energetic electrons around 60–110 km. However, these model studies did not include electron cyclotron motion and did not consider magnetic field effects on electrons.

The purpose of this study is to survey the effects of induced magnetic field structures on diffuse auroral emissions caused by SEP electrons based on a newly developed Monte Carlo model and MAVEN observations. The model description is shown in Section 2. Three sets of the model results are shown in Section 3. Section 3.1 shows the comparison of resultant auroral emission altitude profiles with previous models. Section 3.2 shows results with simple input parameters to investigate the systematic effects of the magnetic field strength and dip angle (angle of the magnetic field from the horizontal direction) on the auroral emissions. Section 3.3 shows the application of the model to the diffuse aurora event in September 2017 with some input parameters based on MAVEN observations. Then discussions and conclusions are presented in Sections 4 and 5, respectively.

2. Model Description and Data Analysis

2.1. Monte Carlo Model

2.1.1. Outline of the Model

In this study, we developed a Monte Carlo model to simulate auroral CO_2^+ UVD emissions caused by electron precipitations into the Martian atmosphere, including the effects of cyclotron motions of the electrons. The Monte Carlo method used in our model is based on Bhardwaj and Jain (2009). The differences between our model and Bhardwaj and Jain (2009) are the atmospheric species, calculation of electron free paths, and some impact cross sections of atmospheric species. Each electron is assumed to be independent, and the energy degradation of each electron is calculated independently.

There are three input parameters to our model: the altitude distributions of CO_2 and O densities in the Martian atmosphere, the magnetic field structures, and the velocity distributions of SEP electrons at the source altitude (set as 300 km altitude in this study), respectively.

The main part of the model calculates the energy loss due to collisions of electrons with CO_2 and O in the Martian atmosphere. Between collisions, each electron motion in the given magnetic field structure is calculated including its cyclotron motion. Namely, at the first step of the main part, we solve the equation of motion for an electron until its collision with a neutral occurs based on the free path of the electron. Then, we decide the colliding neutral atmospheric component by using the ratio between the product values of total cross sections and densities of CO_2 and O. Once the target species is decided, we decide the collisional reaction by using the ratio of cross sections for the reactions of each neutral atmospheric component. Depending on the selected reaction, the electron's velocity after the collision is calculated. Then, we go back to the first step until the electron's energy decreases to below 9 eV where electrons cannot excite the CO_2^+ ($B^2\Sigma_u^+$) producing CO_2^+ UVD emissions when it de-excites to the ground state. For backscattered electrons, the model stops the calculation for the electron when the electron reaches the altitude above the sum of 500 km and 1.1 times electron's gyroradius. If the secondary or higher order electrons are produced, energy degradation of these electrons is also calculated in the same way as originally inputted electrons, after the primary electrons' calculations are finished.

The model output is the altitude distribution of the number of collisions producing excited $CO_2^+(B^2\Sigma_u^+)$. The details of input parameters, calculations, and model outputs are explained in the following subsections.

2.1.2. Electron Motion

From this point on, the detailed calculations of the model are described. The energy of the electrons is lost through collisions with the Martian neutral atmosphere. In this part, we describe the motion of the electrons until they collide with the neutral atmosphere. The equation of motion for an electron is shown as

$$\frac{d\boldsymbol{v}}{dt} = \frac{e}{m_e}\sqrt{1-\beta^2}(\boldsymbol{v}\times\boldsymbol{B})$$

where $\boldsymbol{v}$, e, m_e, β, and $\boldsymbol{B}$ represent the electron velocity, the electron charge, the electron mass, the relativistic Lorentz factor, and the magnetic field, respectively. This equation of motion and the equation for velocity

$$\frac{d\boldsymbol{r}}{dt} = \boldsymbol{v}$$

are solved with a fourth-order Runge-Kutta method, and their results are used to solve the motion of the electron and to determine the distance dS traveled by the electron during one timestep dt.

dS is then used to determine the collision with the neutral atmosphere. The free path is calculated by using a random number R with a range of [0,1] and the following equation.

$$-\ln(1-R) = \int \left(n_{CO_2}(r_z)\sigma_{CO_2}(E) + n_O(r_z)\sigma_O(E)\right) dS$$

n_{CO_2} represents the number density of carbon dioxide molecules, σ_{CO_2} represents the total cross section of carbon dioxide molecules, n_O represents the number density of oxygen atoms, σ_O represents the total cross section of oxygen atoms, r_z represents the z component of electron position, and E represents electron energy. The right side of this equation increases as time progresses. A collision occurs when the value on the right side is equal to or greater than the value on the left side, and the free path is determined by integration of dS. The method for determining the timestep d is shown below.

First, to ensure a description of the cyclotron motion, the timestep was set to 1/180 of the electron cyclotron period. For this purpose, we use the following inequality:

$$dt < \frac{2\pi}{180}\omega_c$$

where ω_c is the electron cyclotron frequency.

Then, to ensure that the number density of the neutral atmosphere does not change significantly in the micro interval, we use the following inequality:

$$dt < \frac{1.0 \times 10^2 \, [\text{cm}]}{v \, [\text{cm}/s]}$$

where v is the electron velocity. The length of 1.0×10^2 [cm] used in inequality is small enough compared to the scale height of neutral atmosphere of CO_2 and O used in Gérard et al. (2017) which is up to $\sim 10^5$ [cm].

Then, to ensure that dS is smaller than the free path estimated with constant atmospheric density and electron energy, we use the following inequalities:

$$FP = \frac{-\ln(1 - R)}{n_{CO_2}(r_z)\sigma_{CO_2}(E) + n_O(r_z)\sigma_O(E)}$$

$$dt < \frac{FP}{v} \frac{1}{100}$$

where FP represents the free path with constant atmospheric density and electron energy.

Finally, since dt is zero when R = 0, we set the minimum value by the following inequality.

$$dt > \frac{1.0 \, [\text{cm}]}{v \, [\text{cm}/s]}$$

We determine dt so that all of the above conditions are satisfied.

2.1.3. Cross Sections

Our model can solve the electron transport in the atmosphere composed of CO_2 molecules and O atoms. CO_2 molecules and O atoms are dominant species of the Martian atmosphere at lower and higher altitudes, respectively.

2.1.3.1. CO_2 Cross Sections

For CO_2, the cross sections are calculated via the equations of Bhardwaj and Jain (2009). The kinds of reactions are the same as the Bhardwaj and Jain (2009). The exceptions which are not calculated by the equations of Bhardwaj and Jain (2009) are the total cross section, the elastic cross section, the elastic differential cross section, and the total ionization cross section. We use the equation of Shirai et al. (2001) for the total CO_2 cross section as in Gérard et al. (2017).

We use the following equation for the elastic cross section.

$$\sigma(E) = \frac{1}{A_1 + B_1 E} + \frac{1}{A_2 + B_2 E} + \frac{2}{E} \frac{\sqrt{A_1 A_2}}{A_2 B_1 - A_1 B_2} \ln\left(\frac{1 + \frac{B_1 E}{A_1}}{1 + \frac{B_2 E}{A_2}}\right) \left[\mathring{A}^{-2}\right]$$

In this equation, the parameters are shown as below.

$$A_1 = 6.9 \times 10^{-2} \left[\mathring{A}^{-2}\right]$$

$$B_1 = 3.7 \left[\mathring{A}^{-2} \, \text{keV}^{-1}\right]$$

$$A_2 = 0.55 \left[\mathring{A}^{-2}\right]$$

$$B_2 = 4.2 \times 10^{-1} \left[\mathrm{\mathring{A}}^{-2} \, \mathrm{keV}^{-1} \right]$$

We calculated these parameters to agree with the cross-section values up to 1,000 eV shown in Itikawa (2002). Our calculated cross section gets close to the value calculated by the parameters shown in Zecca et al. (1995) for 20–4,000 eV electrons as the electron energy increases.

For the elastic differential cross section, the equation of Porter et al. (1987) is used for the electron energy above 1,000 eV. In this calculation, the backscattering term is ignored because forward scattering is dominant for higher electron energy (Porter et al., 1987; Yalcin et al., 2006). We calculate the scattering angle probability based on elastic differential cross sections in the electron energy 10 keV, 100 keV, and 1,000 keV, which are interpolated linearly for energies in between.

The total ionization cross section above electron energy 84028.7 eV is calculated by the equation of Rieke and Prepejchal (1972), which was fitted to the measurements of 0.1–2.7 MeV electron energy. The value 84028.7 eV is set to keep the continuity of the total ionization cross section of Bhardwaj and Jain (2009). Comparison between the two cross sections is shown in Figure S1 and Text S1 in Supporting Information S1.

2.1.3.2. O Cross Sections

For O atoms, the cross section of Alves et al. (2016) is used for the oxygen elastic cross section less than 30 eV. For the oxygen elastic cross section more than or equal to 30 eV, the same fitting equation as the CO_2 elastic cross section is used with the cross-section value of Alves et al. (2016). The parameters are shown as below.

$$A_1 = 1.9 \times 10^2 \left[\mathrm{\mathring{A}}^{-2} \right]$$

$$B_1 = 1.1 \times 10^{-3} \left[\mathrm{\mathring{A}}^{-2} \, keV^{-1} \right]$$

$$A_2 = 0.19 \left[\mathrm{\mathring{A}}^{-2} \right]$$

$$B_2 = 2.3 \times 10^{-3} \left[\mathrm{\mathring{A}}^{-2} \, keV^{-1} \right]$$

The elastic differential cross section is calculated by the equation of Porter et al. (1987) in the same way as CO_2. We calculate the scattering angle probability based on elastic differential cross sections, and they are interpolated linearly in the same way as CO_2.

The inelastic cross sections, which include excitations, Rydberg states, and ionizations, are calculated by the equations of Jackman et al. (1977), except the nonrelativistic Equation 2 of Jackman et al. (1977). The cross sections corresponding to the Equation 2 of Jackman et al. (1977) are calculated by the Equation 5 of Porter et al. (1976), which is the relativistic equation, instead.

2.1.4. Outputs of the Model

Since altitude profiles of the diffuse auroras were obtained along the line-of-sight in the limb geometry, we calculated the limb line-of-sight integration of the auroral altitude profile in the same way as Haider and Masoom (2019). We ignore the horizontal variability of precipitating electron flux, magnetic field strength, dip angle, and atmospheric profiles, and assume that the altitude profiles of the auroral emissions are horizontally uniform. Because the auroral intensities reported by Schneider et al. (2018) are the mean values between 50 and 100 km altitude, we also calculate mean limb intensities between 50 and 100 km altitude.

CO_2^+ UVD is emitted by the transition from the $CO_2^+(B^2\Sigma_u^+)$ state to the ground state. The branching ratio from the $CO_2^+(B^2\Sigma_u^+)$ state to the ground state is set at 0.5, which is the same value used in previous research (Bhardwaj & Jain, 2013; Fox & Dalgarno, 1979; Haider & Masoom, 2019; Nakamura et al., 2022).
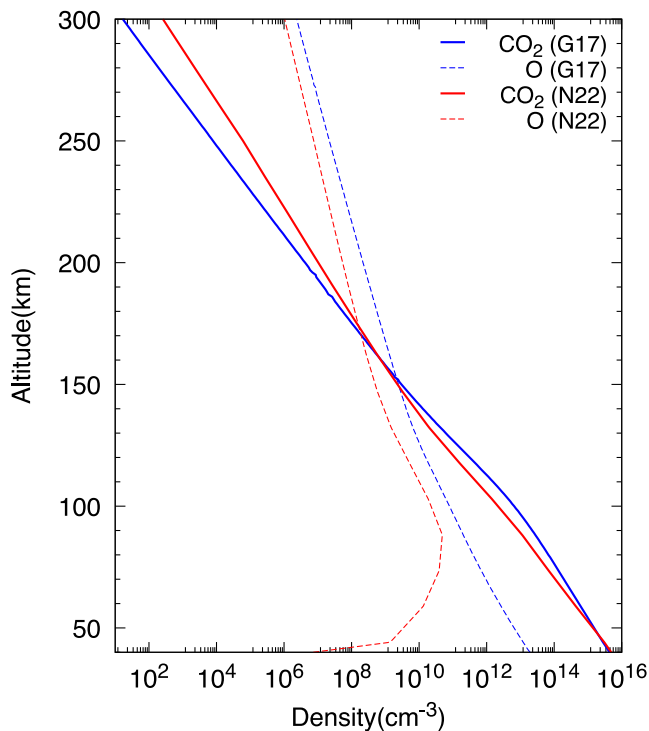
Figure 1. Neutral density profiles used in our model calculations. Blue lines show the model density profiles for December 2014 auroral events used by Gérard et al. (2017), shown as G17 in the caption. Red lines show the model density profiles for the 13 September 2017 auroral events used by Nakamura et al. (2022), shown as N22 in the caption. Solid and dotted lines show the CO_2 and O atmospheric density profiles, respectively.

2.2. Input Parameters

2.2.1. Neutral Atmosphere

We use two cases of neutral atmospheric density profiles as shown in Figure 1. One case of the neutral atmosphere inputs (blue lines in Figure 1) is the same as those used in Gérard et al. (2017) to simulate the December 2014 auroral events. These density profiles are calculated by M-GITM (Bougher et al., 2015) at local time 24:00, latitude 62.5°N, Ls 270°, Flare F10.7, and Solar flux index on the Earth 160. This case is used to compare our model to the model result of Gérard et al. (2017) for validation purposes. The other case of neutral atmosphere inputs is the same as those used in Nakamura et al. (2022). These profiles are calculated by the Mars Climate Database version 5.3 (Millour et al., 2018) to reproduce the atmospheric density profiles on 13 September 2017. We use this case of the neutral atmosphere inputs to investigate the effect of magnetic fields on Martian diffuse auroras and the application of the model to the September 2017 event.

2.2.2. Background Magnetic Fields

We use uniform magnetic field structures to qualitatively investigate the magnetic field dip angle and strength effects on Martian diffuse auroras. We simulated under several magnetic field strengths and dip angles to examine the magnetic field effects. The dip angle is defined as the angle between a horizontal axis and the magnetic field line. The magnetic field lines in our simulation are directed toward the Martian ground for every dip angle.

In Section 3.1, we validate the collisional physics in our model to compare it with Gérard et al. (2017) and Nakamura et al. (2022), which ignored magnetic fields. For this purpose, the magnetic field strength is set to 10 nT, and the dip angle is set to 90° (perpendicular to the surface), which results in the same altitude profiles of auroral emissions without magnetic fields in a plane-parallel atmosphere.

To examine the magnetic field effects from Section 3.2, the magnetic field strength is set to 10 or 100 nT, and the dip angle is set to 10–90° in 10-degree increments. For the use of the observational data, the magnetic field strength is selected from the four fixed values (10, 30, 50, and 100 nT) closest to the observational magnetic field strength from the MAVEN MAG magnetic field vector measurements (Connerney et al., 2015) L2 data during the 2017 diffuse auroral event. We selected the data in the altitude range of 275–325 km close to the initial altitude of electrons in our model (300 km), and we averaged them for each path. The dip angles are set to artificial two constant values, 10 or 90°, to estimate the maximum effects of dip angles. We did not use the observational data for dip angles because the observational data in 275–325 km altitude range during the 2017 diffuse auroral event are limited on the dayside due to the spacecraft orbit, and the dip angles on the nightside auroral region should be different from the dayside observations.

For magnetic field intensity, the actual nightside magnetic field intensity will be different from the dayside (Crider et al., 2003), and it is difficult to know the correct magnetic field intensity in each location. In this study, we focused on reflecting the global magnetic field intensity trend caused by solar wind dynamic pressure on our model instead of local variations. Our rough allocation of magnetic field intensity fulfills this purpose.

2.2.3. Electron Distribution Function at the Upper Boundary

Our model needs the incident electron flux for each incident electron energy bin and the electron pitch angle distribution at the electrons' initial altitude of 300 km. We first calculate the auroral emission profiles normalized by the incident electron flux of 1 cm^{-2} s^{-1}, which is multiplied by the incident electron flux to obtain the flux-weighted auroral emission profile. The incident electron number is 10,000 for each incident energy and each magnetic field configuration shown in following paragraphs.

For model validation in Section 3.1, we use the same setting as Gérard et al. (2017): the incident electron energies are set to 2, 4, 10, 20, 35, 60, 100, 150, or 200 keV, and the downward flux at each energy is set to 1 mW m^{-2}. The pitch angle distributions are isotropic in the range from 0 to 90°.

To examine the magnetic field effects in Section 3.2, the incident electron energy is set to 100 keV, and the downward flux is set to 1 mW m^{-2}. The pitch angle distributions are isotropic in the range from 0 to 40° based on observations, as shown in Figures S2–S4 and Text S2 in Supporting Information S1. We also checked the SEP pitch angle distributions during other events and confirmed that the field-aligned dominant PADs were observed around 300 km altitude also in nightside.

For the event study in Section 3.3, we used the L2 data of the electron flux measurements obtained by the MAVEN SEP instrument, and we applied the same incident electron energy bins to the model as the MAVEN SEP instrument (21.0497, 22.4964, 23.9430, 26.1130, 29.0062, 32.6228, 37.6860, 44.1959, 52.8757, 64.4487, 79.6384, 99.8912, 126.654, 161.373, and 206.942 keV) (Larson et al., 2015). We added the incident energy bins from 10 to 20 keV with 1 keV increment to take into account the lower energy electrons' effects. The pitch angle distributions are isotropic in the range from 0 to 40°.

We used two altitude ranges: 275–325 km altitude for the SEP flux in the ionosphere and above 5,000 km altitude for SEP electron flux in the magnetosheath. The MAVEN SEP instrument consists of four detectors, and each instrument has the attenuator to protect the instrument (Larson et al., 2015). Because the attenuator states of ON (closed) and OFF (open) affect the sensitivities of instruments, we chose the data at the timing when all the attenuators are in the same state for 275–325 km altitude range data. For the SEP flux data above 5,000 km, we do not set the attenuator state criteria and show the data for the whole time period as a reference. The data are averaged between 4 SEP instruments for each altitude range passage. As an exception, only for the comparison of our results to the observational auroral altitude profile as shown in Figure 5d, we ignore the altitude criteria and use the timing criteria which is the same time of auroral observation (02:28:35–02:43:19 on 13 September 2017). The altitude range is 2,651–3,368 km in this case.

SEP electron flux data in 275–325 km altitude are the dayside data and will be different from the nightside exact flux values where auroras occur. However, lower altitude data are useful to infer the flux variations from outside to inside of the induced magnetosphere. Therefore, we used both altitude ranges for flux data. The auroral data calculated with SEP electron flux above 5,000 km altitude will be upper limit of auroral emissions.

Since the MAVEN SEP measurements provide differential flux data (cm^{-2} s^{-1} sr^{-1} keV^{-1}), we multiply them with energy bin widths, solid angles, and the auroral emission intensity altitude profiles normalized at 1 cm^{-2} s^{-1}. The energy bin width of each incident energy channel is determined by half the difference of energy bin between adjacent channels' energy. The energy bin width of each edge channel is determined by the difference of energy bin between the adjacent channel and the edge channel. Solid angles are set to 4π at 275–325 km altitude because averaging 4 SEP instruments leads to ignoring the field-aligned Mars-ward distribution of electrons in lower altitude. The solid angles are set to 2π above 5,000 km altitude and the SEP flux for Figure 5d.

We estimated the differential flux below 24 keV because of the lower sensitivity of the instrument (Larson et al., 2015). We assume that the differential flux below 24 keV is constant and equal to the differential flux observed in the 26 keV bin by the MAVEN SEP instrument. Note that because this assumption does not change the trends of our main results, the effects of magnetic field structures on Martian diffuse auroras, we use this method where the lower energy bands without observations do not contribute to the auroral emissions significantly.

2.3. IUVS Data Analysis

We used the MAVEN IUVS L1C data for the CO_2^+ UVD emission profiles (Jain et al., 2015; Schneider et al., 2018). The L1C files for the aurora/nightglow observations are different from those typically delivered at the PDS that contain only dayside airglow emissions. For the nightglow/aurora observations, we only include nitric oxide (NO), CO Cameron, Solar continuum, CO_2^+ UVD, and OI 297.2 nm model templates in the multi-linear regression model to calculate the radiance (Stevens et al., 2015). We use side segment inlimb and outlimb data in our study as in Schneider et al. (2018) (L1b are available at PDS). The L1c files used in this study are publicly available at CU Scholars (https://doi.org/10.25810/ejx3-5167).

We calculate the mean auroral intensity between 50 and 100 km altitude to compare the observational results to our model results. The data sometimes include minus intensities because of over-subtractions of background noises.

3. Results

3.1. Model Validation

We compare our results to the previous diffuse auroral model study by Gérard et al. (2017). We used the model validation case inputs described in Section 2. The results are shown in Figure 2. The vertical axes are the altitude, and the horizontal axes are the volume production rate of CO_2^+ UVD with 1 mW m^{-2} downward electron flux, which is equal to the condition of Figure 6a of Gérard et al. (2017).

In Figure 2a, we show the calculated CO_2^+ UVD emission profiles using the atmospheric density altitude profile used in Gérard et al. (2017) shown in Figure 1. We compare our peak altitudes to those shown in Figure 6a of Gérard et al. (2017). The peak altitudes well matched within 5 km discrepancies below 35 keV incident electron energy. At higher electron energies, the peak altitude discrepancies increase with increasing the incident electron energies. Our peak altitudes are higher than the peak altitudes of Gérard et al. (2017). Our peak altitude of 200 keV incident electron energy is greater than the peak altitude of Gérard et al. (2017) by about 10 km. Our peak altitude at 100 keV is 71.5 km, which is lower than the simulated peak altitude of 78 km for 100 keV electrons for the same SEP event in December 2014 by Nakamura et al. (2022). Therefore, our peak altitudes at electron energies higher than 35 keV are intermediate between previous two models. We think that the differences of our model results from previous models come from different cross sections or model calculation scheme.

The peak intensity at lower incident electron energies agrees with Gérard et al. (2017). Our peak intensity is $9.7 \times 10^2 \ (\mathrm{cm}^{-3} \ \mathrm{s}^{-1})$ at 2 keV, while the peak intensity of Gérard et al. (2017) at the same energy is about $9.9 \times 10^2 \ (\mathrm{cm}^{-3} \ \mathrm{s}^{-1})$. Our peak intensity decreases with increasing the incident electron energy. This trend is the same as Gérard et al. (2017), but the decrease rate of our model is more gradual than Gérard et al. (2017). This gradual trend is also confirmed by Nakamura et al. (2022), who attributed the gradual trend to the strong forward scattering for elastic collisions at higher energies. Our peak intensity is $6.8 \times 10^2 \ (\mathrm{cm}^{-3} \ \mathrm{s}^{-1})$ at 200 keV, while the peak intensity of Gérard et al. (2017) at the same energy is about $8.4 \times 10^1 \ (\mathrm{cm}^{-3} \ \mathrm{s}^{-1})$. There is a discrepancy by a factor of 8 between our model and Gérard et al. (2017) at 200 keV. The discrepancies in the peak intensity at higher energies are possibly caused by the strongly forward elastic scatterings in our model, which was discussed by Nakamura et al. (2022). The strongly forward elastic scatterings result in weak back scatterings, and weak back scatterings increase auroral intensities.

We check the dependence of the simulated auroral emission profiles on neutral atmospheric density profiles. Figure 2b shows the altitude profiles of volume emission rates of the CO_2^+ UVD using different neutral atmospheric profiles shown in Figure 1. Solid and dotted lines represent the applied atmospheric profiles same as Gérard et al. (2017) and Nakamura et al. (2022), respectively. The peak intensities are almost identical, while the peak altitudes differ depending on the applied atmospheric density profiles. The differences are 7 km for 20 keV, 6 km for 100 keV, and 5 km for 200 keV. The peak altitudes using the atmospheric density profiles of Nakamura et al. (2022) are lower than the peak altitudes using those of Gérard et al. (2017). Less atmospheric density in the former case than in the latter case below 150 km altitude results in lower stopping altitudes. These two cases of the atmosphere (September 2017 and December 2014) correspond to the northern summer and southern summer seasons, respectively, highlighting the contrast in the atmospheric density profiles between the atmospheric contraction and inflation seasons. Therefore, atmospheric profiles affect the altitude of auroral emissions, but not the peak intensity.

3.2. Magnetic Field Effects

We show the altitude profiles of the auroral emissions with 100 nT magnetic field strength and various dip angles in Figure 3a. The energy of incident electrons is fixed at 100 keV, and the downward flux is 1 mW m^{-2}. Figure 3a shows that the smaller dip angles result in broader auroral emission profiles in altitude. We define three characteristic altitudes, a peak altitude, a lower 1/e altitude, and an upper 1/e altitude. A peak altitude represents the altitude where the auroral emission intensity is maximum. A lower or upper 1/e altitude represents the lower or upper altitude where the auroral emission intensity equals 1/e of the maximum intensity, respectively.
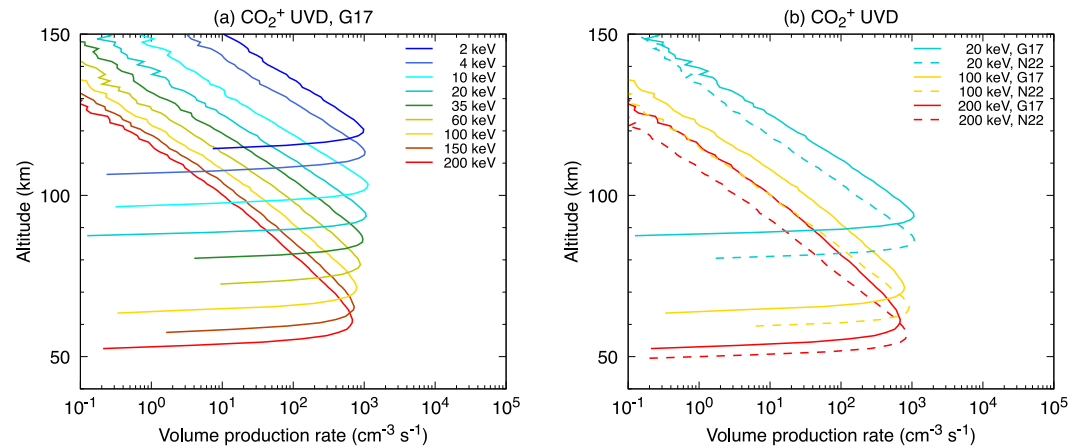
Figure 2. Altitude profiles of the CO_2^+ UVD volume emission rate. (a) The profiles are calculated with the atmospheric density profiles used in Gérard et al. (2017) (referred to as G17) to compare and validate our model. (b) The profiles are calculated with two different atmospheric density profiles used in Gérard et al. (2017) and Nakamura et al. (2022) (referred to as N22) to estimate the dependence on the atmospheric density profile.

We show the peak altitudes, lower 1/e altitudes, and upper 1/e altitudes with magnetic field strengths of 10 and 100 nT in Figure 3b. In both magnetic field strength cases, peak, lower 1/e, and upper 1/e altitudes increase as dip angles decrease. This result indicates that more horizontal magnetic fields allow brighter emission at higher altitudes. In the 100 nT case, peak and upper 1/e altitudes vary up to 13 and 16 km by variation of dip angles, respectively. In 10 nT case, peak and upper 1/e altitudes vary up to 5 and 11 km by variation of dip angles, respectively. Comparing different magnetic field cases at the same dip angles, the peak and upper 1/e altitudes vary up to 9 and 5 km, respectively. These results indicate that dip angle variations affect the auroral emission altitude profiles especially at high altitudes more than magnetic field strength variations.

Figure 3c shows the variations of mean limb intensity in the 50–100 km altitude range depending on the dip angle and strength of magnetic fields. Figure 3c shows that greater dip angles result in weaker mean limb intensities. This is because a smaller dip angle leads to a broader auroral emission altitude profile, and integrating the broader emission altitude profile by altitude makes brighter emissions. This mechanism will be discussed in Section 4. The Dip angle variations cause 26% and 15% mean limb intensity variations in the 100 and 10 nT cases,
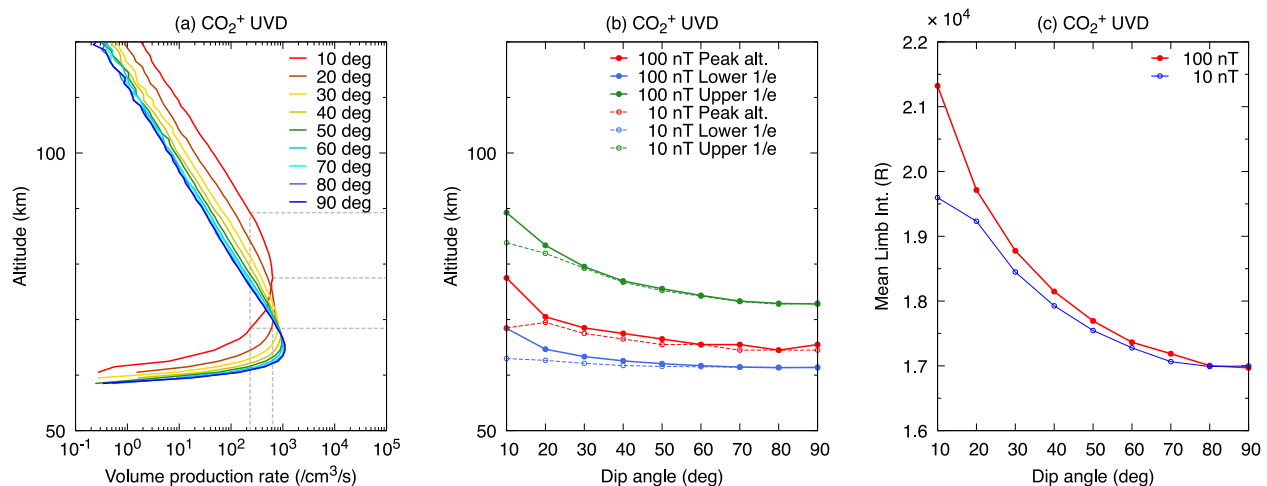
Figure 3. (a) Volume emission rate of CO_2^+ UVD in 100 nT case. (b) Their peak altitudes and upper and lower 1/e altitudes. The peak altitudes, lower 1/e altitudes, and upper 1/e altitudes are shown in panel (b) as red lines, blue lines, and green lines, respectively. Solid and dotted lines represent 100 and 10 nT magnetic field intensity cases, respectively. The vertical axis shows the altitude, and the horizontal axis shows the dip angle. (c) The mean limb intensities in 50–100 km. The horizontal axis shows the dip angle, and the vertical axis shows mean limb CO2+ UVD intensity within 50–100 km altitude. The red and blue lines show 100 and 10 nT cases, respectively.

respectively. Comparing the same dip angle and different magnetic field strength cases, the mean limb intensity variations are up to 8.8%. These results indicate that dip angle variations affect the mean limb intensity of the auroral emissions more than magnetic field strength variations.

3.3. Event Study

Figure 4 shows MAVEN observational SEP flux data, MAVEN observational magnetic field strength and dip angle, two different dip angle cases of model calculated auroral mean limb intensity, MAVEN observational auroral mean limb intensity, and the ratio of auroral intensity between the two dip angles cases. Figures 4a and 4b show the SEP ion flux above 5,000 km altitude and in 275–325 km altitude, respectively. These ion fluxes are shown just for the references, and they are not used for the inputs of our model. Figures 4c and 4d show the SEP electron flux above 5,000 km altitude and in 275–325 km altitude, respectively. The SEP electron fluxes shown in Figures 4c and 4d are used as input for our model calculations. Figures 4e and 4f show magnetic field strength and dip angle, respectively. Only the magnetic field strength shown in Figure 4e at each timing is used as input for our model calculations. The way to use magnetic field strength data as inputs is shown in Section 2. Note that we set the fixed dip angles because the MAVEN observations in 275–325 km altitude are limited only on the dayside due to the MAVEN orbit in this event, and the dip angle data measured on the dayside cannot be used to infer the dip angle on the nightside where auroras occur. Therefore, we used two fixed values for the dip angle, 90 and 10°.

Figure 4g shows the mean limb intensity of CO_2^+ UVD in 50–100 km altitude observed by MAVEN IUVS for both the outlimb and inlimb observations. Each data point represents the mean value per one swath. The emission peak was 7.6 kR at 02:46 on 13 September 2017. After the peak, the mean intensity decreases with time. At around 07:27 on 16 September 2017, there was a slight increase in auroral intensity.

Figure 4h shows the model mean limb intensity in 50–100 km altitude with fixed dip angle 90° (blue) and 10° (red). The auroral emission intensities of the two altitude range cases for the SEP electron flux are similar, but a higher altitude input case results in a more stable temporal variation of the auroral emission intensity. The mean limb intensity of the 10° case is greater than that of the 90° case. This feature is consistent with that of the simple case shown in Figure 3c. The emission peak is 5.8 kR at 03:13 on 13 September 2017. After the peak, the mean intensity decreases with time, but there are intensity fluctuations for the model calculated auroral emissions with 275–325 km SEP electron flux. These fluctuations correspond to the SEP electron flux variations in 275–325 km altitude.

Figure 4i shows the ratio of the model calculated mean limb intensity with 10° dip angle to that with 90° dip angle. The ratios of the two altitude range cases for the SEP electron flux are similar, but a higher altitude input case results in a more stable temporal variation. The mean ratio of the mean limb intensity in 50–100 km altitude is about 1.13 for both altitude input cases shown in Figure 4i. The effect of dip angles on the auroral mean limb intensity in 50–100 km is about 13% in the uniform magnetic field structures.

Figure 4j also shows the ratio of the mean limb intensity between the two dip angle cases as Figure 4i, but the altitude range is changed from 50–100 km to 75–100 km. The ratios of the two altitude range cases for the SEP electron flux are similar, but a higher altitude input case results in a more stable temporal variation. The mean ratio of the mean limb intensity in 75–100 km altitude is about 1.83 for lower altitude input case (1.80 for higher altitude input case), that is, the different dip angles result in a ∼83 (80)% variation in the 75–100 km altitude case.

To investigate the dependence of auroral emission intensity on the SEP electron flux changing in time, we picked up three timespans. The three timespans are shown in Figure 4 as a bold line and two boxes. The first timespan shown (bold line in Figure 4) is 02:28:35–02:43:19 on 13 September 2017. This timespan is the same timing of the vertical profile of the CO_2^+ UVD limb intensity published in Schneider et al. (2018). The second timespan shown as a dotted box is 00:00–12:00 on 16 September 2017. The third timespan shown as a dashed box is 00:00–12:00 on 18 September 2017. The second and third timespans are the decreasing phase.

Figures 5a–5d show the observational SEP electron energy flux, a schematic picture for our model calculations, and the limb-integrated auroral intensity altitude profiles calculated by our model, respectively. The numbers of the lines, 1, 2, and 3, correspond to the timespans shown in Figure 4, 02:28:35–02:43:19 on 13 September 2017, 00:00–12:00 on 16 September 2017, and 00:00–12:00 on 18 September 2017, respectively. The flux data shown in Figure 5a is the mean data in each timespan, which is used to calculate auroral emission profiles in each timespan in Figures 5c and 5d.
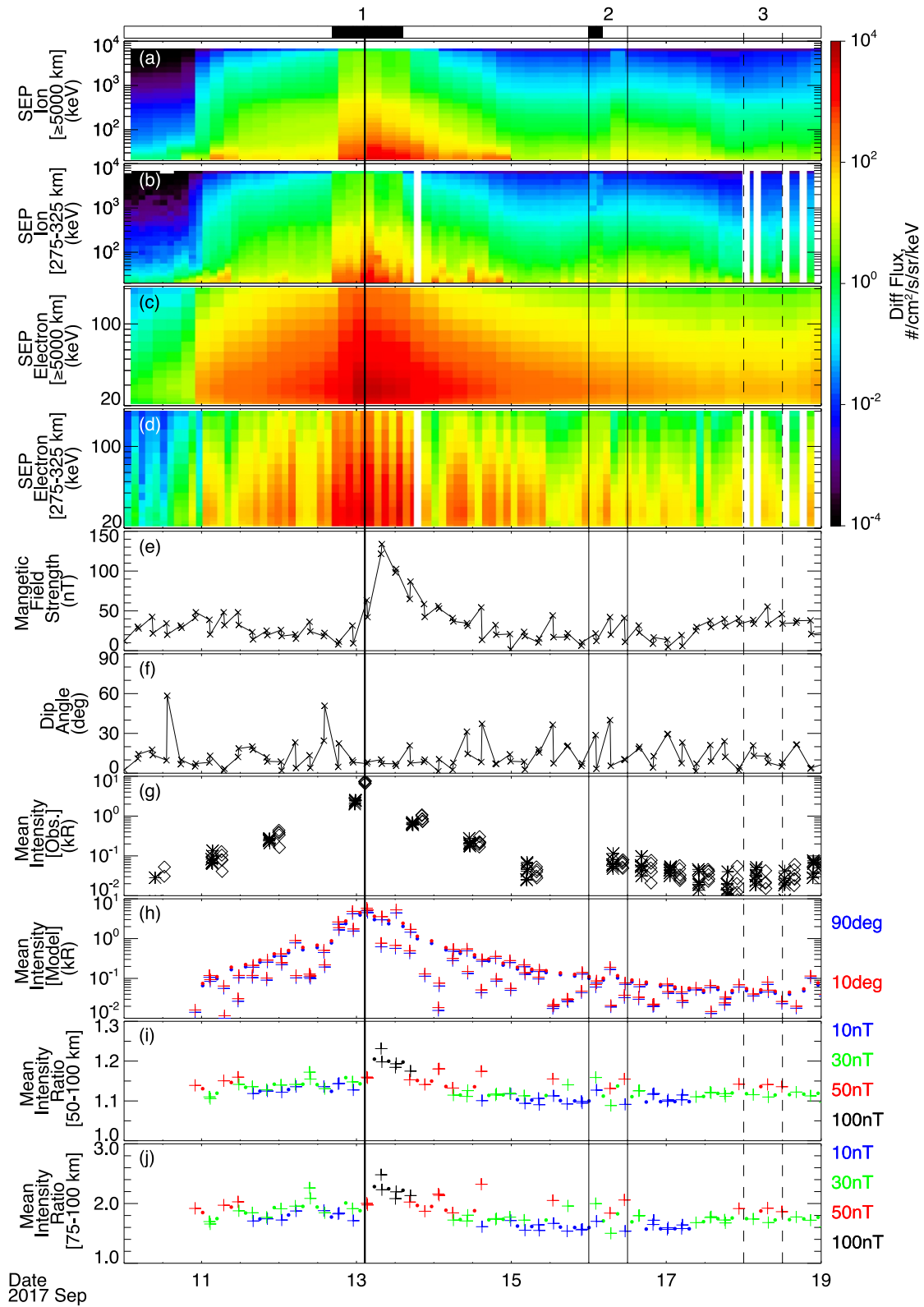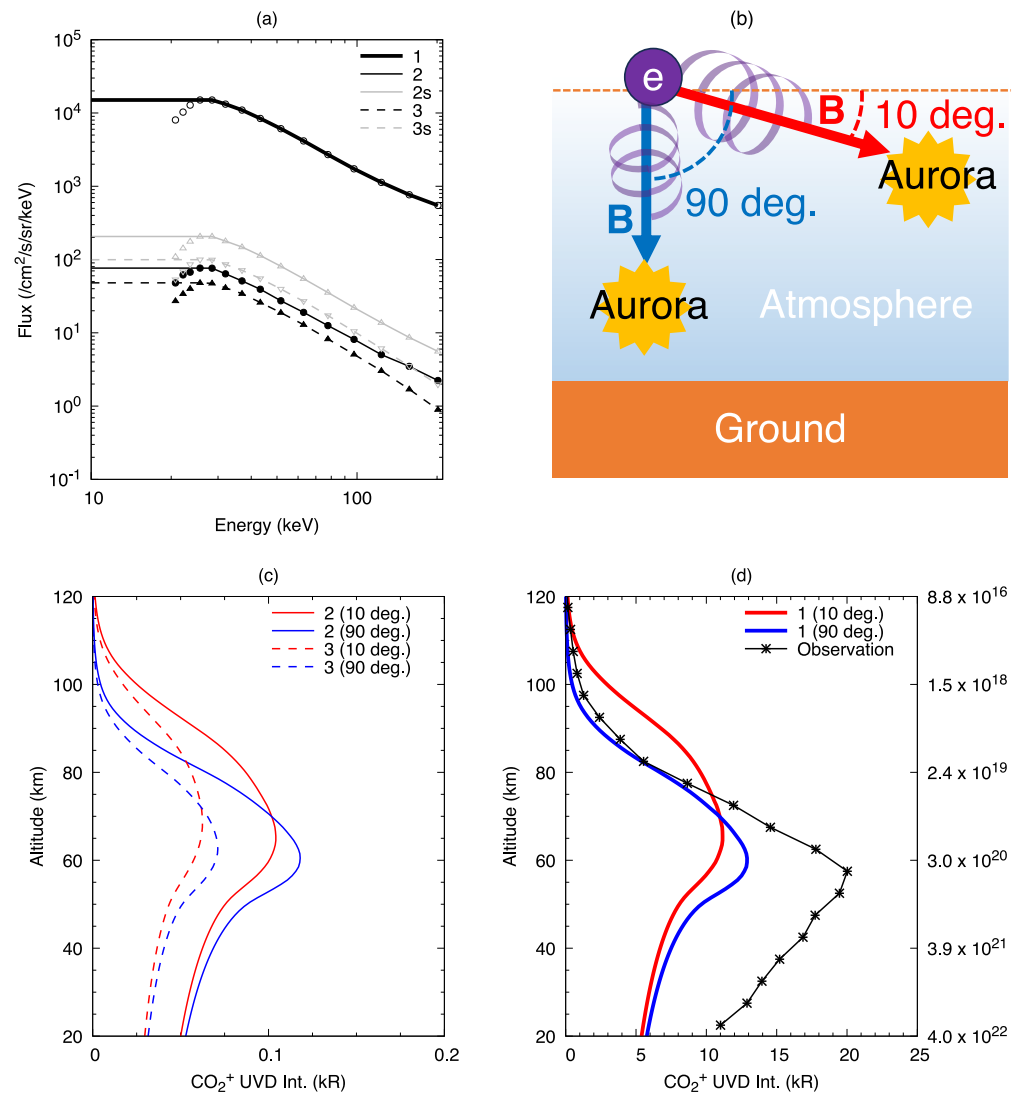
Figure 4.

Figure 5. Results for the three timespans in Figure 4. (a) solar energetic particles (SEP) electron flux in 275–325 km altitude (black), in sheath region set to greater than or equal to 5,000 km altitude (gray). The points represent the observational values by MAVEN/SEP, and the lines represent the input flux for our model. (b) The schematic picture of our model calculations. The red and blue arrows represent the magnetic fields with dip angle 10 and 90°, respectively. (c) CO_2^+ UVD limb integrated emission altitude profile with dip angle 10° (red lines) and 90° (blue lines). The input SEP electron flux is 275–325 km altitude range. (d) Comparison of our model calculated CO_2^+ UVD limb integrated emission altitude profile to the MAVEN IUVS observation shown in Schneider et al. (2018) (black line and points). The bold, solid, and dotted line styles and line numbers represent the timespan corresponding to the line styles and number of boxes in Figure 4. "1" (bold) is 02:28:35–02:43:19 on 13 September 2017, "2" (dotted) is 00:00:00–12:00:00 on 16 September 2017, and "3" (dashed) is 00:00:00–12:00:00 on 18 September 2017.

Figure 4. (a–g) Time series of MAVEN observations and (h–j) our model calculation results. (a) Solar energetic particles (SEP) ion flux above 5,000 km altitude. (b) SEP ion flux in 275–325 km altitude. (c) SEP electron flux greater than or equal to 5,000 km altitude. (d) SEP ion flux in 275–325 km altitude. (e) Magnetic field strength in 275–325 km altitude. (f) Dip angle of magnetic field in 275–325 km altitude. (g) IUVS/MAVEN observational mean limb intensity of CO_2^+ UVD in 50–100 km altitude. The asterisk and diamond symbol shapes represent the outlimb and inlimb observations, respectively. (h) Model calculated mean limb intensity of CO_2^+ UVD in 50–100 km altitude. The blue and red points represent the results with dip angle 90 and 10°, respectively. (i) Ratios of mean intensity with 10- and 90-degrees dip angles in 50–100 km altitude, and (j) Ratios of mean intensity with 10- and 90-degrees dip angles in 75–100 km altitude. The cross and circular symbol shapes in (h–j) represent the input SEP electron flux in 275–325 km and greater than or equal to 5,000 km altitude, respectively. The numbers, "1," "2," and "3," above the Figure represent the time to show the SEP electron flux and auroral emission altitude profiles in Figure 5. The top black boxes represent the timespan when the attenuator is closed during 275–325 km observations.

In Figure 5a, the electron flux in 275–325 km altitude (black lines) is less than that above 5,000 km (gray lines), so the SEP electron flux decreases as it gets close to the Mars. Comparing the three timespans, the SEP electron fluxes in both higher and lower altitudes decrease as the timespans get later.

Comparing the two different dip angle cases in the same timespan in Figure 5c, the smaller dip angle leads to the broader limb emission altitude profile. The broader limb emission altitude profile contributes to the brighter mean auroral intensity in the altitude ranges of 50–100 km and 75–100 km as shown in Figures 4i and 4j, which is the same mechanism shown in Figure 3c. The difference in auroral intensity between the two dip angle cases increases with higher altitude, which leads to higher mean intensity ratios between the two dip angle cases shown in Figure 4j.

The calculated auroral emission intensity decreases from the second to the third timespan comparing the same dip angle case because the input electron flux decreases over time. However, the auroral emission intensity of timespan 3 with a dip angle of 10° is greater than that of timespan 2 with a dip angle of 90° in an altitude above 82.5 km. This result suggests that the auroral emission intensity altitudes are largely affected by the magnetic dip angles, not just the precipitating SEP electron fluxes.

In Figure 5d, we compared our model results (red and blue lines) to auroral emission altitude profile around the emission peak timing observed by MAVEN IUVS (Black line) (Schneider et al., 2018). The peak intensity of our result is 11–13 kR and that of the observation is 20 kR. The peak altitudes of our model results are 60.5 km with a dip angle of 90° (blue line) and 65.5 km with a dip angle of 10° (red line), while the observational peak altitude is 57.5 km. Our models underestimate the auroral emission intensity below 72.5 km. Above 77.5 km, the observed auroral emission intensities are within the model results of 90 and 10° dip angle cases. The altitude range where the dip angle affects the auroral emission altitude profiles strongly depends on the Martian neutral atmosphere changing in season, so the height-integrated neutral density from 300 km altitude at the upper boundary of the model is shown in the right vertical axis as a reference.

4. Discussion

The shape of the model auroral emission altitude profile depends on the dip angle rather than the magnetic field intensity especially at higher altitudes as shown in Figure 3a. This is because the dip angle changes the slant path of electrons. Electrons on more horizontal magnetic fields go through a longer distance per unit altitude, and this leads to more collisions between electrons and neutral atmosphere at higher altitudes than in the case of more vertical magnetic fields shown as Figure 5b. Through this mechanism, auroral emission altitude profiles especially at higher altitudes are changed by magnetic fields. This mechanism has less to do with electrons' exact gyroradii than dip angles. Therefore, the dip angles have more effects on auroral altitude profiles than magnetic field intensities.

The mean limb intensity of the auroral emissions varies with the magnetic field dip angle, but this does not mean that the energy conservation is broken. The variations result from the line-of-sight limb integration. In the limb integration, higher altitude emissions contribute much to the limb integrated emissions because the limb auroral emission intensity at a certain altitude is derived from the integration of the auroral emissions at altitudes higher than that altitude along the line-of-sight in limb geometry. In other words, the emissions at a given altitude are added to the limb integration at altitudes below that altitude. Since higher altitude emissions are added more to the mean limb intensity than lower altitude ones, a broader emission profile before the limb-integration leads to a brighter limb-integrated emission intensity even if the total height-integrated intensities before limb-integration are the same. In fact, the auroral emission altitude profiles before limb-integrations become broader with smaller dip angle as shown in Figure 3a. These emission variations do not appear in nadir integrated emissions because nadir integrations reflect the total energy degradations of incident electrons. The nadir integrated emissions are more proper values to discuss the energy conservations. In our simulation results, the mean nadir intensity in the timespan of Figures 4i and 4j varies with dip angles by ∼ 0.8%, while the mean limb emission intensity in 50–100 km altitude is ∼13%. Therefore, our model obeys the energy conservation.

The temporal variations of the mean limb emission intensity of our model results shown in Figure 4h are consistent with those of MAVEN IUVS shown in Figure 4g. The peak timing is quite similar. The difference in the peak timing derives from the difference in the observation timings. Our model outputs are limited by the timing when the MAVEN spacecraft exists in 275–325 km or above 5,000 km altitude for the input of our model.

MAVEN IUVS observations are conducted at different timings than our SEP input fluxes. The mean intensities of our model results have quite similar values to those of MAVEN IUVS, despite the difference in the timings between our model and observations. In addition, our model mean intensity slightly increases at 06:35 on 16 September 2017, which is consistent with slight increase of observational mean intensity. This slight increase results from the SEP electron flux enhancement as seen in Figure 4d. However, we need to pay attention to these results because the observational data are close to MAVEN IUVS threshold.

We underestimated the auroral emission intensity below 72.5 km. This is possibly because we ignored SEP proton precipitations. Nakamura et al. (2022) pointed out that the SEP protons around or above a few MeV contribute more to lower peak emissions than the SEP electrons around hundreds of keV. SEP protons around or above a few MeV can make up for the underestimated auroral emissions in lower altitudes. Above 77.5 km, the observational intensities are sandwiched between 90 and 10° dip angle cases. This infers that the local dip angle where aurora was observed is an intermediate case. However, please note that there is ambiguity for the higher altitude auroral emissions due to ambiguity in the lower energy electron flux. We assume the energy-independent SEP flux for the lower energy below 24 keV as shown in Figure 5a. This assumption is reasonable because the fluxes have intermediate values between observations and power law fitting values. It is difficult to estimate the real spectrum of electron flux below 24 keV because MAVEN cannot observe this energy range. In this work, we use constant flux for simplicity. For future work, we need the proper fitting way for the lower energy SEP electrons to decrease the ambiguity.

In addition, please note that the SEP electron flux data gained by SEP instruments with closed attenuator state as shown in black boxes at the top of Figure 4 have larger errors than those with opened attenuator state. It leads to larger auroral intensity errors. The errors are caused by data contaminations. There are overestimating factors and underestimating factors for the contaminations. The instrument attenuator closes to reduce the particle flux and avoid saturation, and the flux data are multiplied by a factor of 100 to consider such an effect, leading to a decrement in the signal-to-noise ratio. It leads to an overestimation of flux for higher energy and an underestimation for lower energy because the background noise does not depend on the particle energy. Pulse pileup leads to an overestimation of the particle energy and an underestimation of counts. Cross contamination with electron and proton overlaps leads to an overestimation of counts. The underestimation factors are dead time and false coincidence of signals for the counts and baseline droop caused by many incident particles and many pulses for energy. These contaminations are combined, and the error with a closed attenuator is about a factor of 3 for SEP electron flux. In contrast, the error with opened attenuator is about 50%. Therefore, please note that there are about a factor of 3 ambiguities of calculated auroral intensities with opened attenuator like timespan 1 and partially timespan 2 in Figure 5.

It should be noted that there are some limitations due to the magnetic field structures assumed in this study. We have discussed the variation of auroral intensity by magnetic fields under a uniform magnetic field assumption. The locally uniform magnetic field assumption is reasonable when considering the regions where induced magnetic fields (draped interplanetary magnetic fields) are dominant, since the draped fields are expected to change gradually as shown by global MHD simulations in Figure S5 in Supporting Information S1 (Sakata et al., 2024). A previous MHD simulation study indicates that when strong crustal magnetic field regions in southern hemisphere located in dawn-side, the crustal magnetic field effects on global magnetic field structures are suppressed, and the draped magnetic fields are dominant globally expect for the vicinity of the strong crustal magnetic field regions (Luhmann et al., 2015). This tendency is partially confirmed by statistical data analysis of MAVEN magnetotail observations (Inui et al., 2019). Thus, at least in such a condition, the results of this study are relevant to the diffuse aurora in the negligible crustal magnetic field regions where the draped fields are dominant especially during strong solar wind dynamic pressure condition as in this SEP event, while the further study will be needed for the aurora emissions in the regions where the crustal magnetic fields are dominant and other factors such as the magnetic mirror force can be important (Lillis & Fang, 2015). The effects of more complicated magnetic structure on diffuse aurora are an important subject for future studies.

Another aspect of the limitation due to the uniform magnetic field assumption includes possible overestimation of the auroral emission intensity because non-uniform magnetic fields contribute to escaping electrons. If the magnetic field near the surface of Mars is a "U" like shape and both edges connect to space, electrons can escape along the magnetic field lines, and they do not deposit all energy into the atmosphere. It may also contribute to the auroral variations during stable SEP flux periods. In addition, non-uniform magnetic field structures will make the

magnetic field intensity more important. For example, non-uniform weaker magnetic field structures lead to more chances to cross the magnetic field lines by electrons, and they will change the electron precipitation patterns. However, if electrons are field aligned as shown in Figures S2–S4 in Supporting Information S1, the effects of magnetic field crossing are suppressed, and they will not affect our results greatly.

There is also the limitation for the incident electron flux. In this study, we used the observational SEP electron fluxes as inputs to our simulations. Since we unfortunately do not have the nightside SEP flux data at low altitudes due to the MAVEN orbital configuration during this event, we prepared two proxies of the incident SEP electron flux, that is, observed SEP flux at dayside low-altitudes (275–325 km) and in the upstream region (>5,000 km). It should be noted that Jolitz et al. (2021) pointed out the patchy SEP electron precipitations into the Martian nightside by their model study. If they occur, limb integrated auroral emission altitude profiles will be affected by the positions where auroral emissions occur. This effect also varies auroral altitude profiles and auroral mean intensities.

This study shows the auroral altitude profile and intensity in higher altitude range can be changeable by magnetic field structures despite the same incident SEP electron flux and neutral atmosphere. Even simple change in the magnetic field dip angle can cause variation of the aurora emission at higher altitudes. The results suggest that the magnetic field structure can be an important factor in understanding distributions of Martian diffuse aurora. For the future work, more complicated magnetic field structures should be considered, since even in the pure induced magnetic field regions, the real magnetic field structure is more complicated than our uniform magnetic field assumption in this study. Combination of the newly developed model with global MHD simulation results will be a useful direction for further understanding of the diffuse aurora.

5. Conclusions

We developed a Monte Carlo model solving the electron cyclotron motions to calculate the emission profiles of CO_2^+ UVD during a Martian diffuse auroral event. We assume uniform magnetic field structures in this study. Our model was able to approximately reproduce the auroral emission intensity and altitude profile observed by MAVEN IUVS. In uniform magnetic field structures, the variation of magnetic field dip angle affects the auroral altitude profiles and intensity rather than the magnetic field intensity variation. A smaller dip angle of the magnetic field, that is, a more horizontal magnetic field structure, leads to a broader auroral emission altitude profile. The broader auroral emission altitude profile results in a brighter limb auroral intensity due to the line-of-sight integration in limb geometry. Dip angle can change the auroral emission intensity by about ~13% in 50–100 km and ~83% in 75–100 km altitude. The results suggest that the auroral altitude profiles in higher altitudes can be changeable by magnetic field structures despite the same incident SEP electron flux and neutral atmosphere. The magnetic field structure can be one of the important factors in understanding the Martian diffuse auroras.

Data Availability Statement

The Mars Atmosphere and Volatile EvolutioN (MAVEN) data are available from the NASA Planetary Data System (https://pds.nasa.gov) and the MAVEN Science Data Center (https://lasp.colorado.edu/maven/sdc/public/). We appreciate all the members of the MAVEN mission team. The modeling data supporting the figures presented in this paper are available at Okiyama et al. (2024).

References

Acuña, M. H., Connerney, J. E. P., Ness, N. F., Lin, R. P., Mitchell, D., Carlson, C. W., et al. (1999). Global distribution of crustal magnetization discovered by the Mars Global Surveyor MAG/ER experiment. *Science*, *284*(5415), 790–793. https://doi.org/10.1126/science.284.5415.790

Afonin, V., McKenna-Lawlort, S., Gringauz, K., Kecskemety, K., Keppler, E., Kirsch, E., et al. (1989). Energetic ions in the close environment of Mars and particle shadowing by the planet. *Nature*, *341*(6243), 616–618. https://doi.org/10.1038/341616a0

Alves, L. L., Coche, P., Ridenti, M. A., & Guerra, V. (2016). Electron scattering cross sections for the modelling of oxygen-containing plasmas. *European Physical Journal D*, *70*(6), 1–9. https://doi.org/10.1140/epjd/e2016-70102-1

Bhardwaj, A., & Jain, S. K. (2009). Monte Carlo model of electron energy degradation in a CO_2 atmosphere. *Journal of Geophysical Research*, *114*(11). https://doi.org/10.1029/2009JA014298

Bhardwaj, A., & Jain, S. K. (2013). CO Cameron band and CO_2 + UV doublet emissions in the dayglow of Venus: Role of CO in the Cameron band production. *Journal of Geophysical Research: Space Physics*, *118*(6), 3660–3671. https://doi.org/10.1002/jgra.50345

Bougher, S. W., Pawlowski, D., Bell, J. M., Nelli, S., McDunn, T., Murphy, J. R., et al. (2015). Mars Global Ionosphere-Thermosphere Model: Solar cycle, seasonal, and diurnal variations of the Mars upper atmosphere. *Journal of Geophysical Research: Planets*, *120*(2), 311–342. https://doi.org/10.1002/2014JE004715

Connerney, J. E. P., Acuña, M. H., Ness, N. F., Kletetschka, G., Mitchell, D. L., Lin, R. P., & Reme, H. (2005). Tectonic implications of Mars crustal magnetism. *Proceedings of the National Academy of Sciences of the United States of America*, *102*(42), 14970–14975. https://doi.org/10.1073/pnas.0507469102

Connerney, J. E. P., Espley, J., Lawton, P., Murphy, S., Odom, J., Oliversen, R., & Sheppard, D. (2015). The MAVEN magnetic field investigation. *Space Science Reviews*, *195*(1–4), 257–291. https://doi.org/10.1007/s11214-015-0169-4

Crider, D. H., Vignes, D., Krymskii, A. M., Breus, T. K., Ness, N. F., Mitchell, D. L., et al. (2003). A proxy for determining solar wind dynamic pressure at Mars using Mars Global Surveyor data. *Journal of Geophysical Research*, *108*(A12), 1–10. https://doi.org/10.1029/2003JA009875

Fox, J. L., & Dalgarno, A. (1979). Ionization, luminosity, and heating of the upper atmosphere of Mars. *Journal of Geophysical Research*, *84*(A12), 7315–7333. https://doi.org/10.1029/JA084iA12p07315

Gérard, J. C., Soret, L., Shematovich, V. I., Bisikalo, D. V., & Bougher, S. W. (2017). The Mars diffuse aurora: A model of ultraviolet and visible emissions. *Icarus*, *288*, 284–294. https://doi.org/10.1016/j.icarus.2017.01.037

Haider, S. A., & Masoom, J. (2019). Modeling of diffuse aurora due to precipitation of H+-H and SEP electrons in the nighttime atmosphere of Mars: Monte Carlo simulation and MAVEN observation. *Journal of Geophysical Research: Space Physics*, *124*(11), 9566–9576. https://doi.org/10.1029/2019JA026688

Halekas, J. S., Luhmann, J. G., Dubinin, E., & Ma, Y. (2021). Induced magnetospheres: Mars. *Magnetospheres in the Solar System*, 393–406. https://doi.org/10.1002/9781119815624.ch25

Harada, Y., Gurnett, D. A., Kopf, A. J., Halekas, J. S., Ruhunusiri, S., DiBraccio, G. A., et al. (2018). MARSIS observations of the Martian nightside ionosphere during the September 2017 solar event. *Geophysical Research Letters*, *45*(16), 7960–7967. https://doi.org/10.1002/2018GL077622

Inui, S., Seki, K., Sakai, S., Brain, D. A., Hara, T., McFadden, J. P., et al. (2019). Statistical study of heavy ion outflows from Mars observed in the Martian-induced magnetotail by MAVEN. *Journal of Geophysical Research: Space Physics*, *124*(7), 5482–5497. https://doi.org/10.1029/2018JA026452

Itikawa, Y. (2002). Cross sections for electron collisions with carbon dioxide. *Journal of Physical and Chemical Reference Data*, *31*(3), 749–767. https://doi.org/10.1063/1.1481879

Jackman, C. H., Garvey, R. H., & Green, A. E. S. (1977). Electron impact on atmospheric gases I. Updated cross sections. *Journal of Geophysical Research*, *82*(32), 5081–5090. https://doi.org/10.1029/ja082i032p05081

Jain, S. K., Stewart, A. I. F., Schneider, N. M., Deighan, J., Stiepen, A., Evans, J. S., et al. (2015). The structure and variability of Mars upper atmosphere as seen in MAVEN/IUVS dayglow observations. *Geophysical Research Letters*, *42*(21), 9023–9030. https://doi.org/10.1002/2015GL065419

Jakosky, B. M., Grebowsky, J. M., Luhmann, J. G., Connerney, J., Eparvier, F., Ergun, R., et al. (2015). MAVEN observations of the response of Mars to an interplanetary coronal mass ejection. *Science*, *350*(6261), 1–8. https://doi.org/10.1126/science.aad0210

Jolitz, R. D., Dong, C. F., Rahmati, A., Brain, D. A., Lee, C. O., Lillis, R. J., et al. (2021). Test particle model predictions of SEP electron transport and precipitation at Mars. *Journal of Geophysical Research: Space Physics*, *126*(8), 1–17. https://doi.org/10.1029/2021JA029132

Kallio, E., McKenna-Lawlor, S., Alho, M., Jarvinen, R., Dyadechkin, S., & Afonin, V. V. (2012). Energetic protons at Mars: Interpretation of SLED/Phobos-2 observations by a kinetic model. *Annales Geophysicae*, *30*(11), 1595–1609. https://doi.org/10.5194/angeo-30-1595-2012

Larson, D. E., Lillis, R. J., Lee, C. O., Dunn, P. A., Hatch, K., Robinson, M., et al. (2015). The MAVEN solar energetic particle investigation. *Space Science Reviews*, *195*(1–4), 153–172. https://doi.org/10.1007/s11214-015-0218-z

Lillis, R. J., & Fang, X. (2015). Electron impact ionization in the Martian atmosphere: Interplay between scattering and crustal magnetic field effects. *Journal of Geophysical Research: Planets*, *120*(7), 1332–1345. https://doi.org/10.1002/2015JE004841

Lillis, R. J., Lee, C. O., Larson, D., Luhmann, J. G., Halekas, J. S., Connerney, J. E. P., & Jakosky, B. M. (2016). Shadowing and anisotropy of solar energetic ions at Mars measured by MAVEN during the March 2015 solar storm. *Journal of Geophysical Research: Space Physics*, *121*(4), 2818–2829. https://doi.org/10.1002/2015JA022327

Luhmann, J. G., Dong, C., Ma, Y., Curry, S. M., Mitchell, D., Espley, J., et al. (2015). Implications of MAVEN Mars near-wake measurements and models. *Geophysical Research Letters*, *42*(21), 9087–9094. https://doi.org/10.1002/2015GL066122

Luhmann, J. G., Dong, C. F., Ma, Y. J., Curry, S. M., Xu, S., Lee, C. O., et al. (2017). Martian magnetic storms. *Journal of Geophysical Research: Space Physics*, *122*(6), 6185–6209. https://doi.org/10.1002/2016JA023513

Luhmann, J. G., Zeitlin, C., Turner, R., Brain, D. A., Delory, G., Lyon, J. G., & Boynton, W. (2007). Solar energetic particles in near-Mars space. *Journal of Geophysical Research*, *112*(10), 1–13. https://doi.org/10.1029/2006JE002886

Ma, Y., Fang, X., Halekas, J. S., Xu, S., Russell, C. T., Luhmann, J. G., et al. (2018). The impact and solar wind proxy of the 2017 September ICME event at Mars. *Geophysical Research Letters*, *45*(15), 7248–7256. https://doi.org/10.1029/2018GL077707

McKenna-Lawlor, S., Kallio, E., Jarvinen, R., & Afonin, V. V. (2012). Magnetic shadowing of high energy ions at Mars and how this effect can be simulated using a hybrid model. *Earth Planets and Space*, *64*(2), 247–256. https://doi.org/10.5047/eps.2011.06.039

Millour, E., Forget, F., Spiga, A., Vals, M., Zakharov, V., Montabone, L., et al. (2018). The Mars climate Database (version 5.3). In *Scientific Workshop: "From Mars Express to ExoMars"*.

Nakamura, Y., Terada, N., Leblanc, F., Rahmati, A., Nakagawa, H., Sakai, S., et al. (2022). Modeling of diffuse auroral emission at Mars: Contribution of MeV protons. *Journal of Geophysical Research: Space Physics*, *127*(1), 1–19. https://doi.org/10.1029/2021JA029914

Okiyama, T., Seki, K., Nakamura, Y., Lillis, R. J., Rahmati, A., Larson, D. E., et al. (2024). Dataset of Study of variation mechanisms of the Martian diffuse aurora based on Monte Carlo simulations and MAVEN observations [Dataset]. *UTokyo Repository*. https://doi.org/10.15083/0002010507

Porter, H. S., Jackman, C. H., & Green, A. E. S. (1976). Efficiencies for production of atomic nitrogen and oxygen by relativistic proton impact in air. *The Journal of Chemical Physics*, *65*(1), 154–167. https://doi.org/10.1063/1.432812

Porter, H. S., Varosi, F., & Mayr, H. G. (1987). Iterative solution of the multistream electron transport equation 1. Comparison with laboratory beam injection experiments. *Journal of Geophysical Research*, *92*(6), 5933–5959. https://doi.org/10.1029/ja092ia06p05933

Rieke, F. F., & Prepejchal, W. (1972). Ionization cross sections of gaseous atoms and molecules for high-energy electrons and positrons. *Physical Review A*, *6*(4), 1507–1519. https://doi.org/10.1103/physreva.6.1507

Sakata, R., Seki, K., Terada, N., Sakai, S., & Shinagawa, H. (2024). Effects of an intrinsic magnetic field on ion escape from ancient Mars based on MAESTRO multifluid MHD simulations. *Journal of Geophysical Research: Space Physics*, *129*(5). https://doi.org/10.1029/2023JA032320

Schneider, N. M., Deighan, J. I., Jain, S. K., Stiepen, A., Stewart, A. I. F., Larson, D., et al. (2015). Discovery of diffuse aurora on Mars. *Science*, *350*(6261), 2–7. https://doi.org/10.1126/science.aad0313

Schneider, N. M., Jain, S. K., Deighan, J., Nasr, C. R., Brain, D. A., Larson, D., et al. (2018). Global aurora on Mars during the September 2017 space weather event. *Geophysical Research Letters*, *45*(15), 7391–7398. https://doi.org/10.1029/2018GL077772

Shematovich, V. I., Bisikalo, D. V., & Gérard, J. C. (1994). A kinetic model of the formation of the hot oxygen geocorona 1. Quiet geomagnetic conditions. *Journal of Geophysical Research*, *99*(12), 23217–23228. https://doi.org/10.1029/94JA01769

Shematovich, V. I., Bisikalo, D. V., Gérard, J. C., Cox, C., Bougher, S. W., & Leblanc, F. (2008). Monte Carlo model of electron transport for the calculation of Mars dayglow emissions. *Journal of Geophysical Research*, *113*(2). https://doi.org/10.1029/2007JE002938

Shirai, T., Tabata, T., & Tawara, H. (2001). Analytic cross sections for electron collisions with CO, CO_2, and H_2O relevant to edge plasma impurities. *Atomic Data and Nuclear Data Tables*, *79*(1), 143–184. https://doi.org/10.1006/adnd.2001.0866

Stevens, M. H., Evans, J. S., Schneider, N. M., Stewart, A. I. F., Deighan, J., Jain, S. K., et al. (2015). New observations of molecular nitrogen in the Martian upper atmosphere by IUVS on MAVEN. *Geophysical Research Letters*, *42*(21), 9050–9056. https://doi.org/10.1002/2015GL065319

Strickland, D. J., Bishop, J., Evans, J. S., Majeed, T., Shen, P. M., Cox, R. J., et al. (1999). Atmospheric ultraviolet radiance integrated Code (AURIC): Theory, software architecture, inputs, and selected results. *Journal of Quantitative Spectroscopy and Radiative Transfer*, *62*(6), 689–742. https://doi.org/10.1016/S0022-4073(98)00098-3

Temmer, M. (2021). Space weather: The solar perspective. In *Living reviews in solar physics, living reviews in solar physics* (Vol. 18(1), p. 4). Springer International Publishing. https://doi.org/10.1007/s41116-021-00030-3

Xu, S., Fang, X., Mitchell, D. L., Ma, Y., Luhmann, J. G., DiBraccio, G. A., et al. (2018). Investigation of Martian magnetic topology response to 2017 September ICME. *Geophysical Research Letters*, *45*(15), 7337–7346. https://doi.org/10.1029/2018GL077708

Yalcin, S., Gurler, O., Gultekin, A., & Gundogdu, O. (2006). An analytical expression for electron elastic scattering cross section from atoms and molecules in 1.0 keV to 1.0 MeV energy range. *Physics Letters, Section A: General, Atomic and Solid State Physics*, *356*(2), 138–145. https://doi.org/10.1016/j.physleta.2006.04.037

Zecca, A., Nogueira, J. C., Karwasz, G. F., & Brusa, R. S. (1995). Total cross sections for electron scattering on NO2, OCS, SO2 at intermediate energies. *Journal of Physics B: Atomic, Molecular and Optical Physics*, *28*(3), 477–486. https://doi.org/10.1088/0953-4075/28/3/018